ISSN 1063-4576, Journal of Superhard Materials, 2016, Vol. 38, No. 2, pp. 103–113. © Allerton Press, Inc., 2016.
Original Russian Text © V.I. Ivashchenko, S.N. Dub, P.L. Scrynskii, A.D. Pogrebnjak, O.V. Sobol', G.N. Tolmacheva, V.M. Rogoz, A.K. Sinel'chenko, 2016, published in Sverkhtverdye Materialy, 2016, Vol. 38, No. 2, pp. 40–54.

Nb–Al–N Thin Films: Structural Transition from Nanocrystalline Solid Solution nc-(Nb,Al)N into Nanocomposite nc-(Nb, Al)N/a–AlN

V. I. Ivashchenko[a, *], S. N. Dub[b, **], P. L. Scrynskii[a], A. D. Pogrebnjak[c], O. V. Sobol'[d], G. N. Tolmacheva[e], V. M. Rogoz[c], and A. K. Sinel'chenko[a]

[a] *Frantsevich Institute for Materials Science Problems, National Academy of Sciences of Ukraine, vul. Krzhizhanovs'kogo 3, Kiev, 03680 Ukraine*

[b] *Bakul Institute for Superhard Materials, National Academy of Sciences of Ukraine, vul. Avtozavods'ka 2, Kiev, 04074, Ukraine*

[c] *Sumy State University, ul. Rimskogo-Korsakova 2, Sumy, 40007 Ukraine*

[d] *Khar'kovskii Polytechnic Institute National Technical University, ul. Frunze 21, Khar'kiv, 61002 Ukraine*

[e] *National Scientific Center, Kharkiv Institute of Physics and Technology, vul. Akademichna, 2, Kharkiv, 61108 Ukraine*

**e-mail: ivash@ipms.kiev.ua*

***e-mail: lz@ism.kiev.ua*

Received March 10, 2015

Abstract—Structures and mechanical properties of thin films of the Nb–Al–N system produced by magnetron sputtering of targets from niobium and aluminum in the Ar–N_2 atmosphere have been studied. It has been shown that as the aluminum concentration increases, the structure of a thin film transforms from the nanocrystalline into the nanocomposite one, which consists of nanocrystallites of solid solutions in a matrix of amorphous aluminum nitride. Hardness, elastic modulus, and yield strength of Nb–Al–N thin films have been studied by nanoindentation in the mode of continuous control of the contact stiffness. It has been found that the transition of the structures of Nb–Al–N thin films from the nanocrystalline to the nanocomposite structures results in an increase of hardness and decrease of elastic modulus due to the formation of a thin amorphous interlayer between grains of nanocrystallites. A high hardness to elastic modulus ratio of Nb–Al–N nanocomposite thin films indicates that the films are a promising material for wear-resistant coatings.

DOI: 10.3103/S1063457616020040

Keywords: Nb–Al–N, X-ray structure analysis, thin films, nanoindentation, first-principles calculation.

1. INTRODUCTION

Thin films based on NbN exhibit many interesting properties like high hardness and electrical conductivity, thermostability and chemical inertness [1, 2]. To increase the resistance to oxidation, niobium nitride coatings are alloyed with aluminum. Besides, the incorporation of aluminum atoms into the lattice results in an increase of hardness [3–8] due to the formation of the $Nb_{1-x}Al_xN$ solid solution. It has been found that structures of nanocrystalline thin films depend on the aluminum content. The $Nb_{1-x}Al_xN$ (at $x < 0.45$) thin films are characterized by the B1 structure of the NaCl type with cubic lattices B1–NbN and A1–$Nb_{0.67}Al_{0.33}N$. At $x > 0.71$ there forms the B4 structure of the wurtzite type with a hexagonal lattice. In the $0.45 < x < 0.71$ range there forms a mixture of B1 and B4 structures [6, 7]. The [6] and [7] publications report that Nb–Al–N nanocrystalline thin films were produced by the deposition from the vacuum arc plasma. The high energetics of the deposition process caused the low amorphous phase content of thin films.

In the present study to produce Nb–Al–N nanocomposite thin films that contain nanocrystallites and amorphous matrix, we used the magnetron sputtering. Our studies showed that in magnetron sputtering of niobium and aluminum targets in the nitrogen and argon atmosphere the deposition of nanocomposite thin films consisting of A1-NbN and A1-$Nb_{0.67}Al_{0.33}N$ nanocrystallites in the matrix of amorphous aluminum

nitride took place. To interpret the results obtained, we made the first-principles calculations of the B1-NbN and B1-Nb_2AlN phases, B1-(Nb,Al)N solid solution, and B1-NbN(001)/B1-AlN heterostructure.

2. EXPERIMENT

The Nb–Al–N thin films were deposited onto Si (100) substrates by the direct current sputtering of targets of Nb (99.9%) and Al (99.999) in the argon and nitrogen atmosphere at the following deposition parameters: substrate temperature 350°C, bias voltage on the substrate –50V; flow rates of argon and nitrogen 40 and 13 cm^3/s, respectively; working pressure in the reaction chamber was 0.17 Pa; current supplied onto aluminum target, I_{Al}, was 50, 100, 150, 200, 250, and 300 mA, which corresponded to the discharge power densities 2.9, 5.7, 8.6, 11.4, 13.7, and 17.1 W/cm^2; current supplied onto niobium target–300 mA. Basic pressure in the vacuum chamber was above 10^{-4} Pa, the angle between targets was –45°, the distance from the target to substrate holder was 8 cm. In one deposition four samples were produced: *a*, *b*, *c*, and *d*, which were placed along the substrate holder. Samples of series *a* were placed at the minimum distance from the niobium target; therefore, the niobium concentration in them was maximum and aluminum noticeable less; samples of series *d* were closer than all other to the target of aluminum; samples of series *c* were placed between the targets of niobium and aluminum, but closer to the latter. This approach makes it possible to obtain thin films of ternary nitrides having different chemical compositions in one sputtering. In this paper we present the results of studying the structure and mechanical properties of samples of series *a* and *c*. For comparison we deposited also thin films of pure aluminum nitride and niobium nitride.

The coatings structures were investigated by X-ray diffraction on a DRON-3M diffractometer in the Cu$K\alpha$ radiation. In superposition of complex diffraction profiles we used the expansion into constituting profiles. The substructure characteristics (sizes of crystallites, microdeformation) were defined by the approximation of the diffraction profile shape by the Cauchy function. FTIR absorption spectra were obtained at room temperature in the range from 400 to 4000 cm^{-1} using a TSM 1202 Infraspec spectrometer. The chemical bonds in the films were analyzed by XPS on a FC 2401 device using the Mg$K\alpha$ radiation ($E = 1253.6$ eV). The peaks Au $4f_{7/2}$ and Cu $2p_{3/2}$ with the binding energies 84.00 ± 0.05 and 932.66 ± 0.05 eV, respectively, were used to calibrate the device.

Mechanical testing of thin films was carried out on a Nano Indenter G-200 (Agilent Technology, USA) using a Berkovich indenter with a tip radius of 340 nm (data of the atomic-force microscopy). The nanoindentation was performed in the continuous stiffness measurement mode (CSM). In such tests the voltage, which is supplied onto the loading head, is modulated by a low-amplitude (2 nm) and low-frequency (45 Hz) signal. The nanoindentation in the CSM mode makes it possible to get the dependence of the average contact pressure (ACP) and elastic modulus, *E*, on the indenter displacement in the region of loading. The tests were conducted at the constant strain rate in the contact ($\dot{\varepsilon} = \frac{1}{h}\frac{dh}{dt}$, where *h* is the displacement of the indenter tip, *t* is the time), which was 0.05 s^{-1}. The indention load was increased till the displacement was 200 nm. 10 imprints were made on each sample. The film thickness was defined by a Micron-gamma optical profilometer. The thickness of Nb–Al–N coatings weakly depended on I_{Al} and varied from 0.7 to 0.9 μm.

3. RESULTS AND DISCUSSION

3.1. Structure of Nb–Al–N Thin Films

As samples of series *a* were placed at the minimum distance from the Nb target and at the maximum distance from the Al target, the aluminum contents of these samples were minimum. The revealed diffraction reflexes (Fig. 1) in samples of the *a* series belong to two phases having cubic lattices. The location of diffraction reflexes of the first phase in the divided spectrum (Fig. 2) of the reflex (200) corresponds to the lattice constant close to 0.4385 nm, which is inherent in the lattice of NbN with a low aluminum content (to 5 at %) following the type of substitution; the lattice spacing of the second phase is close to 0.4285 nm, which is characteristic of solid solutions A1-$Nb_xAl_{1-x}N$ with the ratio of niobium and aluminum atoms in the lattice 2 : 1 that corresponds to the formula $Nb_{0.67}Al_{0.33}N$. The latter was defined based on the Vegard law for crystal lattices of the same type in the substitution of atoms with different radii [9]. Thus, samples of thin films of the *a* series are nanocrystalline, consisting of grains of the B1-(Nb, Al)N solid solutions containing B1-$Nb_{0.67}Al_{0.33}N$ and less than 5 at % Al.

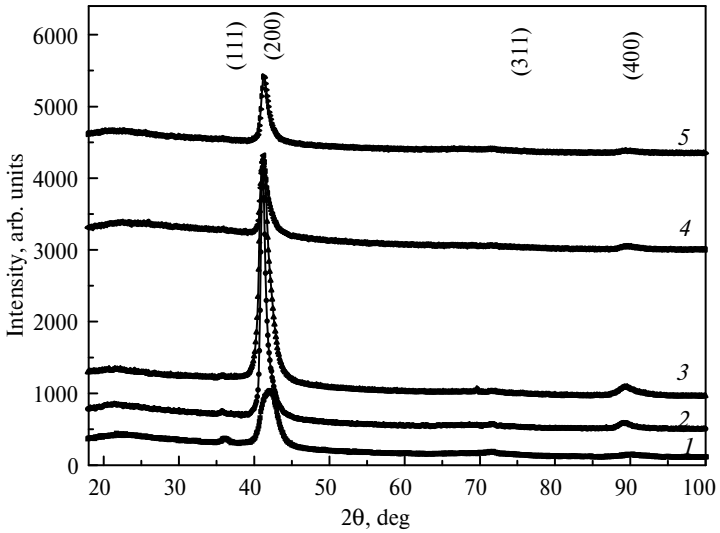

Fig. 1. XRD spectra of Nb–Al–N coatings deposited at I_{Al} = 50 (*1*), 100 (*2*), 150 (*3*), 250 (*4*), 300 (*5*) mA (samples of series *a*).

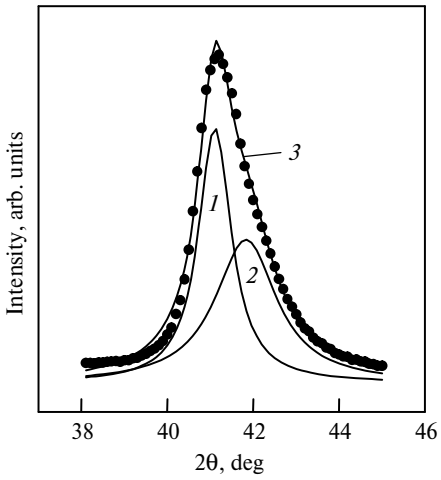

Fig. 2. Region of a diffraction spectrum of the Nb–Al–N coating (series *a*) deposited at I_{Al} = 150 mA with division into constituents of the film reflexes: NbN (*1*), $Nb_{0.67}Al_{0.33}N$ (*2*), accumulation approximating curve (*3*), points indicate the initial data array.

Samples of series *c* were located between the targets, closer to the aluminum target. Therefore, the aluminum contents of these samples should be well above than of samples of series *a*. Figure 3 demonstrates X-ray diffraction spectra of Nb–Al–N films of series *c* produced at different I_{Al} currents. The marked peaks correspond to the B1-NbN structure [6]. A characteristic feature of the spectra is the appearance of a preferred orientation of crystallites on the basis of the B1-NbN phase with substitution of Al atoms for a portion of Nb atoms, which are denoted therefore, as B1-(Nb, Al)N with the [100] axis of the crystallites textures that are perpendicular to the growth plane. The latter is defined in diffraction spectra (see Fig. 2) by the increase of the relative intensities of the (200) and (400) reflexes. The analysis of substructural characteristics made by the approximation of the shape of the diffraction profile by the Cauchy functions showed that with increasing I_{Al} the size of the crystallites of the B1-(Nb, Al)N phase increases in the texture axis direction, which is accompanied by a small amplification of the microdeformation (Table 1). In the separation of complex diffraction profiles of this series coatings into constituents (Fig. 4) it is seen that in parallel with the reflexes of the B1-(Nb, Al)N crystal phase in the 2θ angles interval of 32–38° and 40–46° the diffused halo-like reflexes are revealed, which are characteristic of amorphous-cluster structural state with the size of the region of ordering 2 nm (the methods of the estimation of the regions of ordering sizes is given in [10]). Centers of the angular ranges of identifiable halo-like curves in diffraction spectra correspond to 35° and 43°, which complies with the positions of AlN peaks [6], displaced to the side of the lowest angles as a result of the replacement of the part of aluminum atoms by niobium atoms having higher atomic radius.

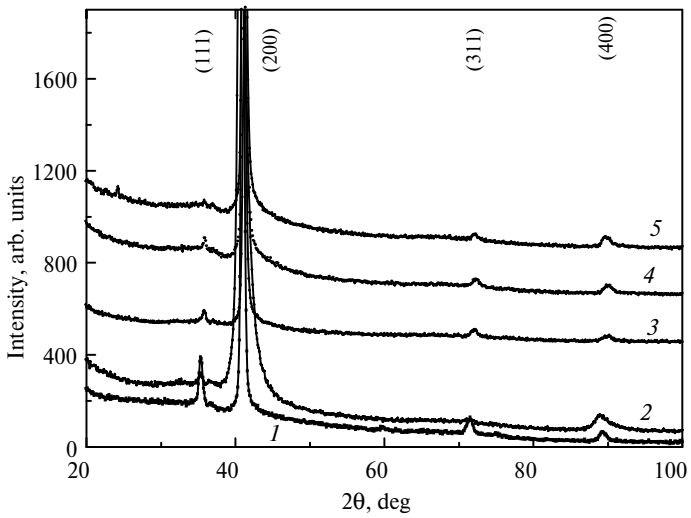

Fig. 3. XRD spectra of Nb–Al–N films (series *c*) deposited at different I_{Al}: 50 (*1*), 150 (*2*), 200 (*3*), 250 (*4*), 300 (*5*) mA.

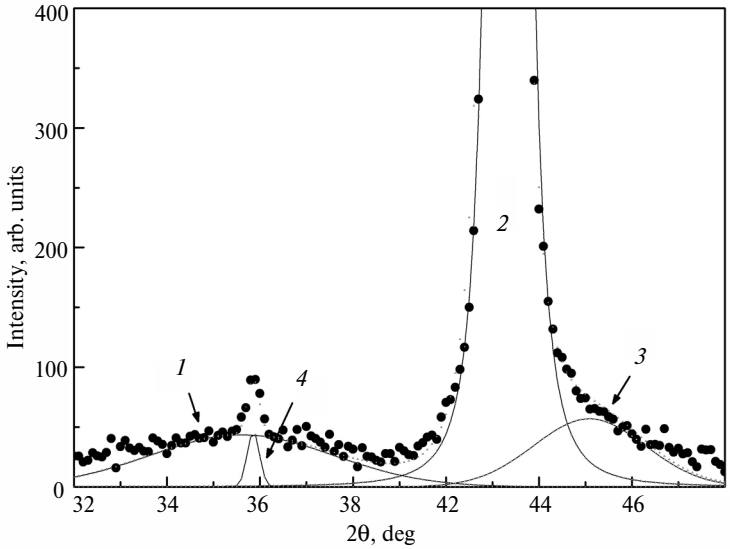

Fig. 4. Region of the diffraction profile with the separation into constituents of the Nb–Al–N film deposited at I_{Al} = 250 mA: *1* and *3* indicate profiles corresponding to halo-like curves of amorphous aluminum nitride, *2* and *4* indicate the peaks corresponding to nanocrystalline B1-(Nb, Al)N (series *c*).

Table 1. Substructural characteristics (average size of crystallites, L, and microdeformation, $\langle\varepsilon\rangle$) of samples of Nb–Al–N nanocomposite thin films of series *c*

$I_{Al,}$ mA	L, nm	$\langle\varepsilon\rangle$, %
50	60	0.14
150	30	0.14
200	70	0.15
250	120	0.15
300	230	0.16

To verify the supposition as to the presence of amorphous aluminum nitride in the samples of series *c*, we deposited thin films at different I_{Al}. The analysis of the X-ray patterns showed that all thin films of aluminum nitride were amorphous (a-AlN). The FTIR spectra of the AlN films are demonstrated in Fig. 5. It is seen that the Al–N bonds intensify with increasing I_{Al}: the absorption zone at 667 cm^{-1} related to the vibrations of Al–N [11] becomes increasingly evident.

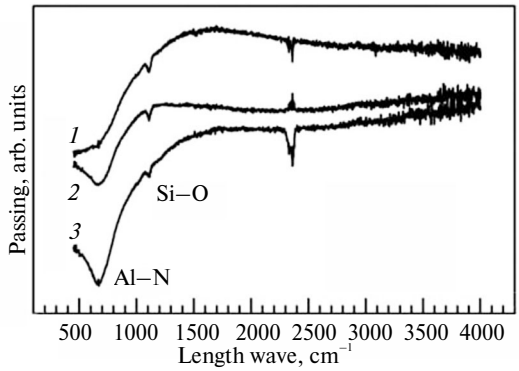

Fig. 5. FTIR spectra of AlN thin films deposited at I_{Al} currents : 150 (*1*), 200 (*2*), 300 (*3*) mA.

However, according to XRD the films remain X-ray amorphous. These data agree with the conclusion about the strengthening of the a-AlN amorphous constituent in thin films of series *c* as the I_{Al} increases.

XPS spectra of spanning levels of Nb–Al–N thin films of series *c* are given in Fig. 6. The spectra were identified using the results reported in [12, 13]. It is seen that Nb–N and Al–N are main bonds in the Nb–Al–N thin films. Thus, the data obtained by XRD, XPS, and FTIR indicate that aluminum nitride is present in thin films of series *c* as an amorphous phase. The Nb–O and Al–O was also revealed in the samples. The presence of these bonds is caused by the fact that a small amount of oxygen is always accumulated in films based on the niobium nitride [5]. According to the XPS measurements, we defined the chemical compositions of films of series *c*. The amounts of niobium, aluminum, nitrogen, and oxygen in the films were ~ 36.3, 12.4, 35.3, and 16.0 at %, respectively. Thus, as the aluminum content increases, the structure of the Nb–Al–N thin films transforms from the nanocrystalline into the nanocomposite one.

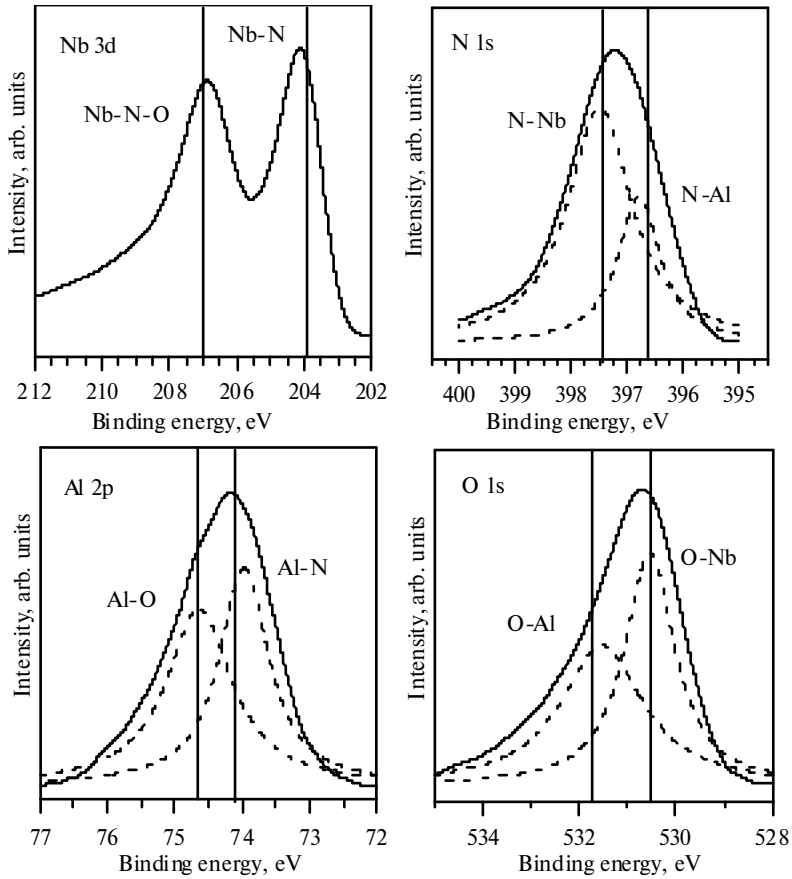

Fig. 6. Typical XRS spectra of spanning levels of Nb–Al–N thin films (series *c*); Gauss components of the spectra are indicated by dotted lines; vertical lines show the corresponding binding energies of atoms according to [11, 12].

3.2. Mechanical Properties

A typical curve of the dependence of the indenter tip displacement, h, on load, P, derived for an Nb-Al–N thin film is given in Fig. 7a. The indenter tip displacement monotonically increases with the indentation load, strain–bursts in the load-displacement curve, which are typical of single crystals, are absent. Also, we should note a high (~ 60%) recovery of the imprint depth in the indenter unloading due to the relaxation of the elastic deformation in the contact, i.e., far in excess than in nanoindentation of metals and alloys. The dependence of the average contact pressure (ACP) on the indenter displacement is shown in Fig. 7b, curve *1*. In the initial region in the displacement range from 0 to 7 nm the deformation of the surface asperities takes place. As the indenter displaces by more than 7 nm, it starts to penetrate into the thin film surface. Up to the point A (h = 28 nm, P = 0.76 mN, ACP = 19 GPa (~0.66 H) the ACP increases in direct proportion to the displacement. Then ACP continues to grow with increased imprint depth but not so fast as in the beginning (the AB region). After point B (h = 81 nm, P = 4.4 mN) the ACP does not longer essentially change with the imprint depth (the BC region). At the displacement above 170 nm (point C) the onset of the hardness decrease due to the effect of a low-modular silicon substrate is observed (elastic modulus is 170 GPa). Therefore, we measured the hardness of Nb–Al–N thin films in the displacement range from 80 to 170 nm. The elastic modulus, E, dependence on the indenter displacement is shown in Fig. 7b (curve *2*). It is seen from the figure that the substrate starts to distort the results of the elastic moduli measurements of thin films at considerably lesser values of the indenter displacements than in the hardness measurements. Therefore, we measured the elastic moduli of thin films in the displacement range from 30 to 60 nm.

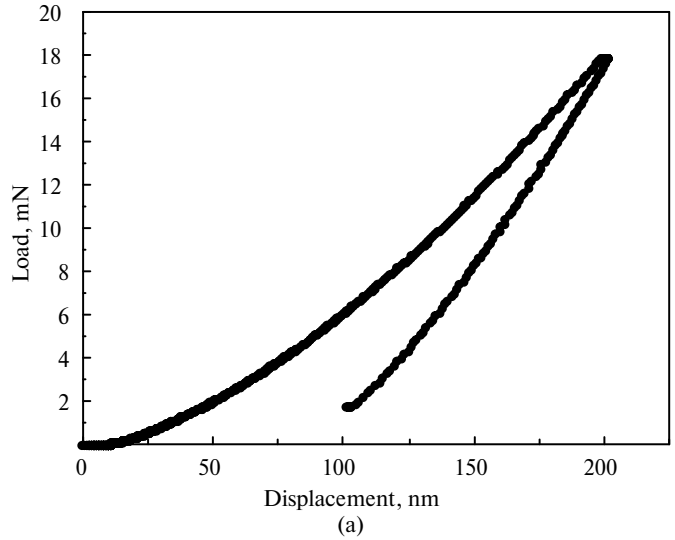

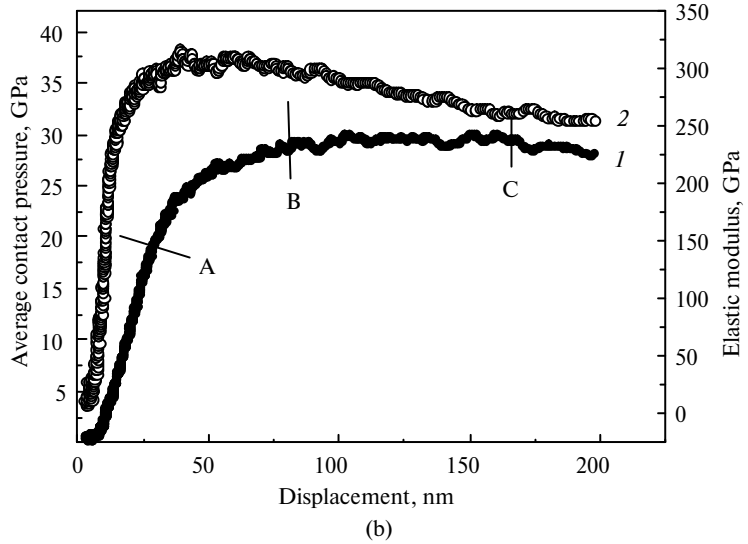

Fig. 7. Load-displacement curve of the indenter (a) and the dependences of ACP (*1*) and elastic modulus (*2*) on the indenter displacement (b).

When analyzing the dependence of the ACP on the displacement it is necessary to remember that the mechanical tests were performed by a Berkovich pyramidal indenter with the tip rounding as a sphere with a radius of ~340 nm. That's why in the range of displacement from 0 to 70 nm the sample surface was deformed by a spherical rounding in the indenter tip. At the displacement above 70 nm a transition to pyramidal indenter begins. The dependence of the ACP on the displacement similar to the given in Fig. 7b, curve *1* was earlier observed by Tabor in penetration of a spherical indenter into a hardened material (a preliminary plastically deformed steel sample) [14]. Tabor explained the observed dependence of the ACP on the displacement, *h*, in the OC region by a change of the deformation mode in a contact. According to Tabor, in the *OA* region only elastic deformation takes place in the contact (see Fig. 7b, curve *1*). At the point A the shear stress under the contact attains a critical value, at which under the imprint a zone of a constraint plastic deformation appears that is surrounded by the elastically deformed material [15]. As the load increases, the size of the zone of a constraint plastic deformation increases, and at the *B* point it intersects the sample surface. At this moment the developed plastic flow starts in the contact (see Fig. 7b, curve *1*). It is known that abrupt elastoplastic transition caused by the homogeneous nucleation of dislocations in the region, which was previously free of dislocations under the contact, is typical of single crystals with low density of structural defects [16]. Earlier a smooth elastoplastic transition was observed for crystalline materials having high densities of dislocations (nanocrystalline and nanocomposite coatings [17, 18] and mechanically polished sapphire single crystals [19]) as a result of the motion and multiplication of dislocations already existing in the contact region.

Thus, the AB section in Fig. 7b is an elastoplastic transition in a contact at the Berkovich indenter penetration into the sample. The ACP, at which the plasticity initiation occurs at nanodeformation of materials by a spherical indenter (point *A* in Fig. 7b) is related to a critical shear stress, τ_c, by the following equation [20]:

$$\tau_c = 0.465 p_c, \quad (1)$$

where p_c is the ACP, at which the plasticity initiation in a nanocontact occurred. Knowing the critical shear stress, we defined the yield strength, Y, using the Mises criterion [20]:

$$Y = \sqrt{3}\tau_c . \quad (2)$$

The results of measurements of the critical shear stress, τ_c, and yield strength, *Y*, of thin films of the Nb–Al–N system at the nanoscale are listed in Table 2. It is seen that the strength properties both of Nb–Al–N nanocrystalline and nanocomposite thin films are noticeably higher than of aluminium nitride and niobium nitride separately. Thus, the nanoindentation makes it possible to measure the strength properties of materials at the nanoscale, including brittle thin films.

Table 2. Elastic modulus, *E*, hardness, *H*, critical average contact pressure of plasticity, p_c, initiation, critical shear stress, τ_c, and yield strength, *Y*, of the Nb–Al–N, thin films measured at nanoindentation

Sample	*E*, GPa	*H*, GPa	*H*/*E*	p_c, GPa	τ_c, GPa	*Y*, GPa	*H*/*Y*
a-AlN	173	12.9	0.075	7.0 ± 0.5	3.3	5.6	2.30
nc-NbN	285	25.1	0.088	15.0 ± 2.2	7.0	12.1	2.07
nc-(Nb, Al)N (sample *a*)	292	26.5	0.091	16.9 ± 0.8	7.9	13.6	1.95
nc-(Nb, Al)N/a-AlN (sample *c*)	276	30.2	0.109	21.9 ± 1.7	10.2	17.6	1.72

Note. The I_{Al} current is 100 mA. For comparison we include the data for thin films of amorphous aluminum nitride and nanocrystalline niobium nitride obtained at the same deposition parameters.

The results of determining the hardness and elastic moduli of thin films of the due to formation of thin layers of amorphous AlN between (Nb,Al)N solid solution nanocrystallites grains Nb–Al–N system, deposited at different currents I_{Al} are given in Fig. 8. It is seen that the hardness and elastic moduli of samples of the Nb–Al–N system increase with the deposition current I_{Al}. The hardness of thin films from amorphous aluminium nitride is minimum (it varies in the range from 12 to 15 GPa). The hardness of nanocrystalline thin films of niobium nitride is much higher ~ 25 GPa (see Table 2). The alloying niobium nitride with aluminium (samples of series *a* and *c*) caused their hardness to increase (see Fig. 8). For samples of series *a* this increase was insignificant, as they were located near the niobium target and contained the minimum amount of aluminium. Their hardness increased to 27 GPa as compared with the 25 GPa of thin films from pure niobium.

From our structural studies it follows that these films are nanocrystalline consisting of nanocrystallites of solid solutions (Nb, AlN)N. Therefore, we can state that the increasing of hardness of series *a* samples is caused by the solid solution strengthening. The increase of the aluminium concentration in Nb–Al–N thin

films (samples of series *c*) essentially affected their mechanical properties. The hardness increased to 31 GPa and elastic modulus decreased as compared with NbN thin films and Nb–Al–N nanocrystalline samples of series *a* (see Fig. 8 and Table 2) due to the formation of thin layers of amorphous AlN between (Nb,Al)N solid solution nanocrystallites grains. Therefore, the H/E ratio for the Nb–Al–N nanocomposite thin films is well above than for nanocrystalline films, i.e., 0.109 and 0.90, respectively.

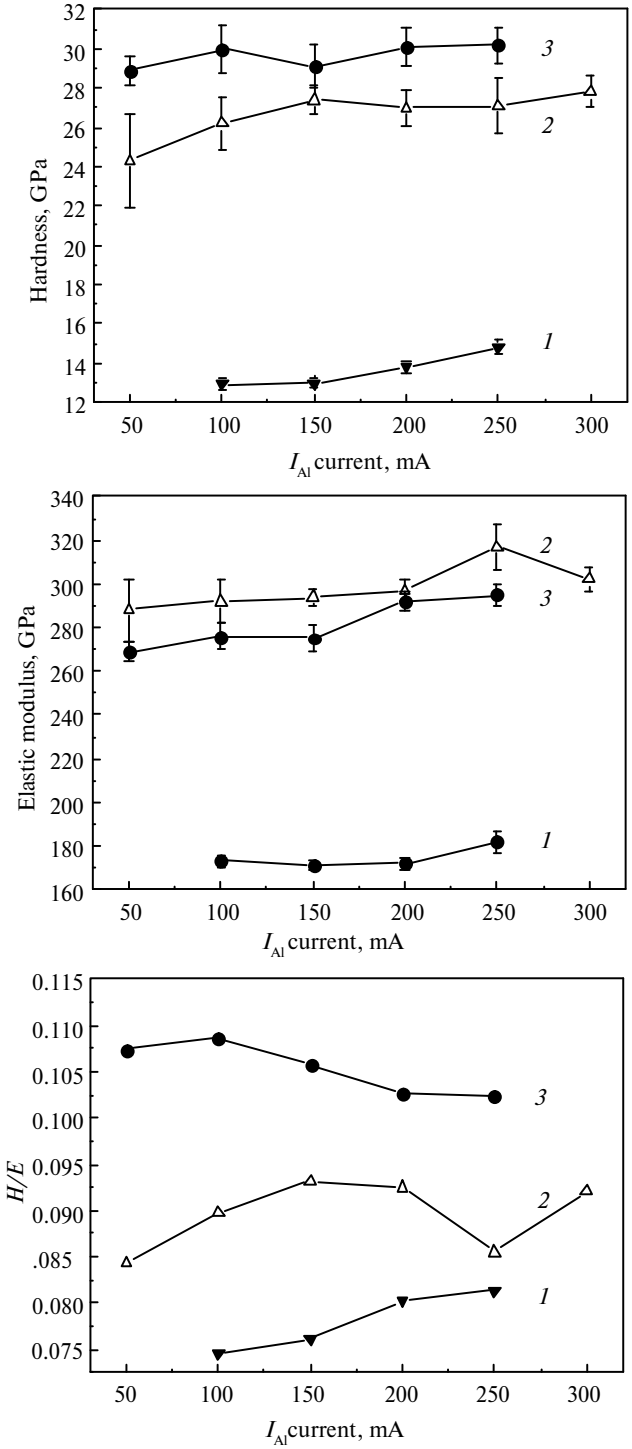

Fig. 8. Nanohardness, H, elastic moduli, E, and the H/E ratios of Nb–Al–N thin films depending on the I_{Al} current a-AlN (*1*), Nb–Al–N nanocrystalline thin film (*2*), Nb–Al–N nanocomposite thin film (*3*).

It is known that the wear resistance of materials is proportional to the H/E ratio. The higher is this ratio, the higher is the wear resistance [21]. Therefore, to increase the wear resistance of materials, it is no need to

tend to a very high hardness. Very hard materials, as a rule, are very brittle and that decreases the wear resistance of them. To increase the H/E ratio, it is important to decrease the elastic modulus. One of the methods to attain this result is to produce nanocomposite materials [21]. The formation of coatings with the nancomposite structure as a rule leads to an increase of the hardness and decrease of the elastic modulus as compared to the nanocrystalline structure [17, 22]. Thus, because of the high H/E ratio the nanocomposite thin films of the Nb–Al–N system are a promising material for wear resistance coatings.

3.3. First-Principles Calculations of the Structures of the Nb–Al–N System

To check the conclusions about the structure of the Nb–Al–N films, we made the first-principles calculations of the B1-NbN phase, B1-$Nb_xAl_{1-x}N$ solid solutions, B1-NbN(001)/B1–AlN heterostructure, and Nb_2AlN ordered phase. The conditions of the calculation are described in detail in [12, 23], the calculations were made using the "quantum-ESPRESSO" [24], the exchange-correlation potential was calculated with the use of the generalized gradient approximation [25]. The simulation in the framework of the molecular dynamics was performed using an NVT assembly at 1400 K with a subsequent cooling to 0 K and static relaxation [23]. We considered 96-atomic structures arranged by translating 8-atomic B1-NbN cell as $(2 \times 2 \times 3)$ [23]. The compositions of solid solutions and heterostructures were chosen to be equal. The Nb_2AlN cell (space group $P6_3/mmc$, No. 194) consists of 8 atoms. The structures we consider include all possible configurations of the $Nb_xAl_{1-x}N$. The XRD spectra are calculated using the PowderCell-2.4 software [26].

Figure 9 shows atomic configurations of B1-NbN(001)/1 ML AlN and B1-NbN(001)/2 ML B1–AlN, where ML is the monolayer, and B1$Nb_xAl_{1x}N$ solid solutions as well. The analysis of total energies of heterostructures and solid solutions shows that the B1$Nb_xAl_{1x}N$ solid solutions at $x < 0.67$ should disintegrate and for these concentrations a nanocomposite structure consisting of B1-NbN and B1-AlN crystallites may form. Using the atomic configurations found as a result of first-principles calculations, we calculated diffraction patterns for the heterostructure B1NbN(001)/2 ML B1AlN and B1NbN, B1$Nb_xAl_{1-x}N$, $x \approx 0{,}67$ and Nb_2AlN phases. The calculated XRD spectra are shown in Fig. 10. It is seen that the formation of a heterostructure or a solid solution should result in an arising of floatings on basic reflections due to cubic niobium nitride at wide angles. This is supported by the measurements results showed in Figs. 1–4. The absence of the peak at $2\theta \approx 32°$ in the experimental diffraction patterns, which is present in the theoretical diffraction patterns of the heterostructure, gives ground to suggest that epitaxial layers of aluminum nitride do not form at the grain boundaries in the films. It follows that the grain boundaries consist mainly of amorphous aluminum nitride, and this agrees with our experiment. We should also mention the fact that the reflection of the Nb_2AlN phase having a hexagonal crystal lattice, which is at $2\theta \approx 38°$ in the calculated pattern (Fig. 10), is absent in the experimental diffraction patterns (see Figs. 1, 3). On the strength of these data one may propose that the films we produced do not contain crystallites of Nb_2AlN hexagonal type and B1-AlN, and aluminum nitride is in films as the amorphous phase.

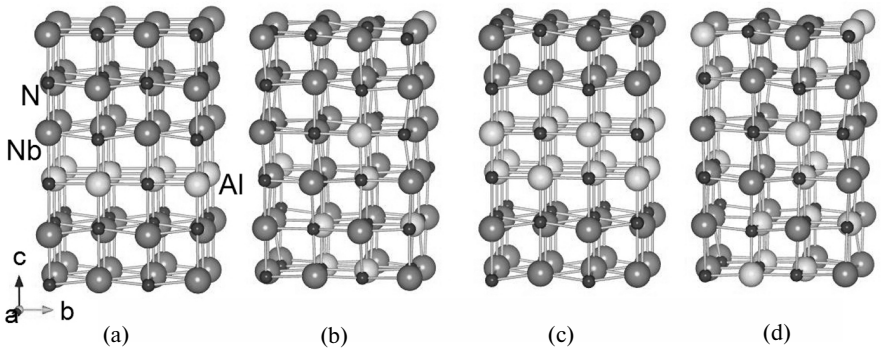

Fig. 9. Atomic configurations of the B1-NbN(001)/1 ML B1-AlN heterostructure (a), the $Nb_{0.83}Al_{0.17}N$ solid solution (b), B1-NbN(001)/2 ML B1-AlN heterostructure (c), and $Nb_{0.67}Al_{0.33}N$ solid solution (d). The compositions of the (a) and (b) structures are the same; the composition of the heterostructure (c) is identical to that of the solid solution (d); the differences of the total energies of the heterostructures and corresponding solid solution with a chaotic arrangement of atoms in the metal lattice are: $E(a) - E(b) = 0.016$ eV/atom, $E(c) - E(d) = -0.039$ eV/atom.

Thus, experimental and theoretical results show that films should consist of crystallites having a cubic crystal lattice B1–NbN and B1-$Nb_xAl_{1-x}N$, $x \approx 0.67$ embedded into the amorphous a-AlN matrix. This conclusion is favored by the fact that for each diffraction peak (200) and (400) the difference in the peak location

$\Delta 2\theta = 2\theta_{(B1\text{-}NbN)}\ 2\theta_{(B1\text{-}NbxAl1-xN)}$ in experimental and theoretic patterns are virtually the same. It should be also noted that films based on niobium nitride are inclined to accumulate a small amount of oxygen [5]. This is also supported by the results of the measurements of the XPS spectra presented in Fig. 6. Oxygen may replace a portion of nitrogen in solid solutions and in the amorphous matrix [27]. Therefore, the $Nb_xAl_{1-x}N_yO_{1-y}$, $x \approx 0.67$, $1 - y << 1$ structure will be more preferable for solid solutions and the a-AlNO structure for the amorphous matrix.

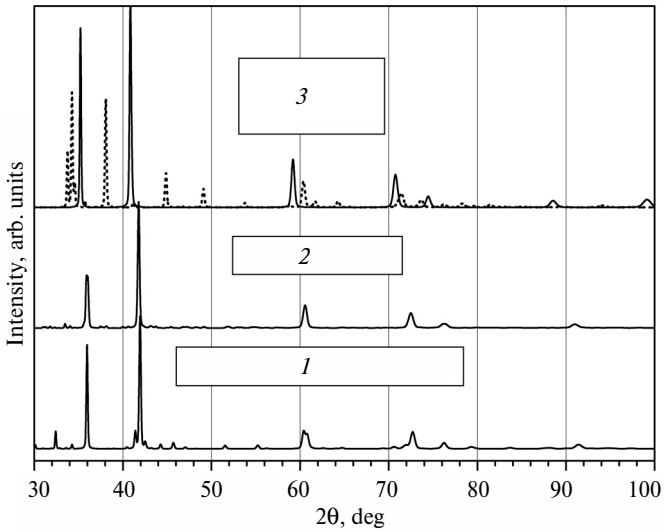

Fig. 10. Calculated X-ray diffraction patterns of the structures: Nb–Al–N: B1-NbN(001)/2 ML B1-AlN (*1*); A1-$Nb_{0.67}Al_{0.33}N$ (*2*); A1-NbN (—) and Nb_2AlN (·····) (*3*).

4. CONCLUSIONS

In studying the Nb–Al–N thin films that have been produced by magnetron sputtering of Nb and Al targets at various currents supplied to the magnetron with the Al target in the I_{Al} range from 50 to 300 mA it has been found that at a low concentration of aluminum there form nanocrystalline thin films with hardness of 26–28 GPa, which consist of nanocrystallites of the A1-(Nb, Al)N and A1-$Nb_{0.67}Al_{0.33}N$ solid solutions. An increase of the aluminum concentration results in the formation of nanocomposite thin films, which composed of the A1-(Nb, Al)N and A1-$Nb_{0.67}Al_{0.33}N$ nanocrystallites and the matrix of amorphous aluminum nitride. The nanohardness of Nb–Al–N nanocomposite thin films varies from 29 to 31 GPa and attains the maximum at the at the I_{Al} current 300 mA. The comparison of the results of the first-principles calculations with the data of experimental studies points to a possibility of the existence of two types of the B1-NbN and A1-$Nb_{0.67}Al_{0.33}N$ crystallites in Nb–Al–N magnetron thin films and the absence of crystalline phases with a noncubic type of the crystal lattice in them. Taking into account the high hardness and H/E ratio of nanocomposite thin films of series *c*, they may be recommended for protective and wear-resistant coatings.

The study is implemented in the framework of the STCU project no. 5964 and complex State programs: Development of science of materials fundamentals of the structural engineering of vacuum-plasma superhard coatings with the aim to achieve the required functional properties and Physical principles of plasma technologies for a complex machining of multicomponent materials and coatings (no. 0113u000137c).

REFERENCES

1. Barnett, S.A., Madan, A., Kom, I., and Martin, K., Stability of nanometer-thick layers in hard coatings, *MRS Bulletin*, 2003, vol. 169, pp. 169–172.
2. Gotoh, Y., Nagao, M., Ura, T., Tsuji, H., and Ishikawa, J., Ion beam assisted deposition of niobium nitride thin films for vacuum microelectronics devices, *Nucl. Instr. Methods Phys. Res. B*, 1999, vol. 148, pp. 925–929.
3. Selinder, T.I., Miller, D.J., and Gray, K.E., Phase formation and microstructure of $Nb_{1x}Al_xN$ alloy films grown on MgO (001) by reactive sputtering: a new ternary phase, *Vacuum*, 1995, vol. 46, pp. 1401–1406.
4. Makino, Y., Saito, K., Murakami, Y., and Asami, K., Phase change of Zr–Al–N and Nb–Al–N films prepared by magnetron sputtering method, *Solid State Phenomena*, 2007, vol. 127, pp. 195–200.
5. Barshilla, H.C., Deepthi, B., and Rajam, K.S., Structure and properties of reactive direct current magnetron sputtered niobium aluminum nitride coatings, *J. Mater. Res.*, 2008, vol. 23, pp. 1258–1268.

6. Franz, R., Lechthaler, M., Polzer, C., and Mitterer, C., Structure, mechanical properties and oxidation behavior of arc-evaporated NbAlN hard coatings, *Surf. Coat. Technol.*, 2010, vol. 204, pp. 2447–2453.
7. Holec, D., Franz, R., Mayrhofer, P.H., and Mitterer, C., Structure and stability of phases within the NbN–AlN system, *J. Phys. D. Appl. Phys.*, 2010, vol. 41, art. 145403.
8. Holec, D., Rachbauer, R., Kiener, D., Cherns, P.D., Costa, P.M. F. J., McAleese, C., Mayrhofer, P.H., and Humphreys, C.J., Towards predictive modelling of near-edge structures in electron energy loss spectra of AlN based ternary alloys, *Phys. Rev. B*, 2011, vol. 83, art. 165122.
9. Jadannadham, K., Sharma, A.K., Wei, Q., Kalyanraman, R., and Narayan, J., Structural characteristics of AlN films deposited by pulsed laser deposition and reactive magnetron sputtering: A comparative study, *J. Vac. Sci. Technol. A*, 1998, vol. 16, pp. 2804–2814.
10. Beresnev, V.M., Torianyk, I.M., Sobol', O.V., Pogrebnyak, A.D., Kropotov, A.Yu., Stervoedov, N.G., Nyemchenko, U.S., Kolesnikov, D.A., and Klimenko, S.A., AlN–TiB_2–$TiSi_2$ coatings obtained by pulsed magnetron sputtering, *Techn. Phys.*, 2014, vol. 59, pp 1220–1223.
11. Rosenberger, L., Baird, R., McCullen, E., Auner, G., and Shreve, G., XPS analysis of aluminum nitride films deposited by plasma source molecular beam epitaxy, *Surf. Interface Anal.*, 2008, vol. 40, pp. 1254–1261.
12. Ivashchenko, V.I., Scrynskyy, P.L., Lytvyn, O.S, Butenko, O.O., Sinelnichenko,O.K., Gorb, L., Hill F., Leszczynski, J., and Kozak, A.O., Comparative investigation of NbN and Nb–Si–N films: Experiment and theory, *J. Superhard Mater.*, 2014, vol. 36, no. 6, pp. 381–392.
13. Umanskii, Ya.S. and Skakov, Yu.A., *Fizika Metallov. Atomnoe stroenie metallov i splavov* (Physics of metals. Atomic structure of metals and alloys), Moscow: Atomizdat, 1978.
14. Tabor, D., Hardness of metals, Oxford: Clarendon Press, 1951.
15. Lysenko, O.G., Dub, S.N., Grushko, V.I., Mitskevich, E.I., and Tolmacheva, G.N., Study of phase transformations in silicon by scanning tunneling spectroscopy and nanoindentation, *J. Superhard Mater.*, 2013, vol. 35, no. 6, pp. 350–355.
16. Zbib, A.A. and Bahr, D.F., Dislocation nucleation and source activation during nanoindentation yield points, *Metall. Mater. Trans. A.*, 2007, vol. 38, pp. 2249–2255.
17. Abadias, G., Koutsokeras, L.E., Dub, S.N., Tolmachova, G.N., Debelle, A., Sauvage, T., and Villechaise, P., Reactive magnetron co-sputtering of hard and conductive ternary nitride thin films: Ti–Zr–N and Ti–Ta–N, *J. Vac. Sci. Technol. A,* 2010, vol. 28, pp. 541–551.
18. Saladukhin, A., Abadias, G., Michel, A., Zlotski, S.V., Uglov, V.V., Tolmachova, G.N., and Dub, S.N., Influence of Al content on the phase formation, growth stress and mechanical properties of TiZrAlN coatings, *Thin Solid Films*, 2013, vol. 538, pp. 32–41.
19. Dub, S.N., Brazhkin, V.V., Belous, V.A., Tolmacheva, G.N., and Konevskii, P.V., Comparative nanoindentation of single crystals of hard and superhard oxides, *J. Superhard Mater.*, 2014, vol. 36, no. 4, pp. 217–230.
20. Johnson, K.L., *Contact mechanics*, Cambridge: Cambridge University Press, 1985.
21. Leyland, A. and Matthews, A. On the significance of the H/E ratio in wear control: a nanocomposite coating approach to optimised tribological behaviour, *Wear*, 2000, vol. 246, pp. 1–11.
22. Lin, J., Moore, J.J., Mishra, B., Pinkas, M., and Sproul, W.D., The structure and mechanical and tribological properties of TiBCN nanocomposite coatings, *Acta Mater.*, 2010, vol. 58, pp. 1554–1564.
23. Ivashchenko, V.I., Veprek, S., Turchi, P.E.A., Shevchenko, V.I., Leszczynski, J., Gorb, L., and Hill, F., First-principles molecular dynamics investigation of thermal and mechanical stability of the TiN(001)/AlN and ZrN(001)/AlN heterostructures, *Thin Solid Films*, 2014, vol. 564, pp. 284–293.
24. Giannozzi, P., Baroni, S., Bonini, N., Calandra, M., Car, R., Cavazzoni, C., Ceresoli, D., Chiarotti, G.L., Cococcioni, M., Dabo, I., Dal Corso, A., De Gironcoli, S., Fabris, S., Fratesi. G., Gebauer, R., Gerstmann, U., Gougoussis, C., Kokalj, A., Lazzeri, M., Martin-Samos, L., Marzari, N., Mauri, F., Mazzarello, R., Paolini, S., Pasquarello, A., Paulatto, L., Sbraccia, C., Scandolo, S., Sclauzero, G., Seitsonen, A.P., Smogunov, A., Umari, P., and Wentzcovitch, R.M., Quantum ESPRESSO: a modular and open-source software project for quantum simulations of materials, *J. Phys.: Cond. Matter.*, 2009, vol. 21, art. 395502.
25. Perdew, J.P., Burke, K., and Ernzerhof, M., Generalized gradient approximation made simple, *Phys. Rev. Lett.*, 1996, vol. 77, pp. 3865–3868.
26. Kraus, W. and Nolze, G., PowderCell for Windows (version 2.4), Berlin, Germany: Federal Institute for Materials Research and Testing, 2000.
27. Ivashchenko, V., Veprek, S., Pogrebnjak, A., and Postolnyi, B., First-principles quantum molecular dynamics study of $Ti_xZr_{1x}N(111)/SiN_y$ heterostructures and comparison with experimental results, *Sci. Tech. Adv. Mater.*, 2014, vol. 15, art. 025007 (11).

Translated by G. Kostenchuk